RESEARCH ARTICLE

Key Points:
- Faults with low reactivation potential slip at maximum injection pressures
- A broad range of fault orientations is activated during periods of high injection rates
- Largest event magnitudes are observed at faults optimally oriented for failure

Supporting Information:
- Supporting Information S1
- Table S1

Correspondence to:
P. Martínez-Garzón,
patricia@gfz-potsdam.de

Impact of fluid injection on fracture reactivation at The Geysers geothermal field

Patricia Martínez-Garzón[1], Grzegorz Kwiatek[1], Marco Bohnhoff[1,2], and Georg Dresen[1,3]

[1]Helmholtz Centre Potsdam GFZ German Research Centre for Geosciences, Potsdam, Germany, [2]Institute of Geological Sciences, Free University Berlin, Berlin, Germany, [3]Institute of Earth and Environmental Sciences, University of Potsdam, Potsdam, Germany

Abstract We analyze the spatiotemporal distribution of fault geometries from seismicity induced by fluid injection at The Geysers geothermal field. The consistency of these faults with the local stress field is investigated using (1) the fault instability coefficient I comparing the orientation of a fault with the optimal orientation for failure in the assumed stress field and (2) the misfit angle β between slip vectors observed from focal mechanisms and predicted from stress tensor. A statistical approach is applied to calculate the most likely fault instabilities considering the uncertainties from focal mechanisms and stress inversion. We find that faults activated by fluid injection may display a broad range in orientations. About 72% of the analyzed seismicity occurs on faults with favorable orientation for failure with respect to the stress field. However, a number of events are observed either to occur on severely misoriented faults or to slip in a different orientation than predicted from stress field. These events mostly occur during periods of high injection rates and are located in proximity to the injection wells. From the stress inversion, the friction coefficient providing the largest overall instability is $\mu = 0.5$. About 91% of the events are activated with an estimated excess pore pressure <10 MPa, in agreement with previous models considering the combined effect of thermal and poroelastic stress changes from fluid injection. Furthermore, high seismic activity and largest magnitudes occur on favorably oriented faults with large instability coefficients and low slip misfit angles.

1. Introduction

Geological exposures of earthquake rupture planes reveal structural details such as roughness, subsidiary faults, and geological slickensides allowing deciphering fault kinematics. In the absence of direct observations, particularly at seismogenic depth, earthquake focal mechanisms allow to reveal the kinematics of seismic fault slip. The long-term structural evolution of faults involves the accumulation of seismic and aseismic slips. However, the crustal stress field controlling fault growth may change locally and in time. For example, studies from major faults as the San Andreas Fault, USA, [*Hardebeck and Hauksson*, 2001] or the North Anatolian Fault Zone, Turkey, [*Örgülü*, 2011; *Ickrath et al.*, 2015] presented spatiotemporal transients of regional stresses using focal mechanisms and stress inversion. Also, large angles (>50°) between fault planes and maximum horizontal stress orientation S_{HMAX} have been found at major fault zones [e.g., *Hardebeck and Hauksson*, 2001; *Townend et al.*, 2012; *Martínez-Garzón et al.*, 2015] suggesting low-frictional fault strength [*Zoback et al.*, 2011].

Recently, there has been an increase in the seismicity induced by human activities such as injection of wastewater in disposal wells, hydraulic fracturing, or geothermal production [e.g., *Ellsworth*, 2013; *Weingarten et al.*, 2015]. The analysis of induced seismicity allows studying deformation in geological reservoirs related to stimulation and production [e.g., *Chen and Shearer*, 2011; *Martínez-Garzón et al.*, 2014; *Barbour*, 2015; *Kwiatek et al.*, 2015]. Induced earthquakes from reactivated faults and fractures with varying orientation are commonly related to perturbations of reservoir fluid pressures and temperatures [*Barton et al.*, 1995; *Shapiro et al.*, 2003; *Rutqvist et al.*, 2013; *Boyle and Zoback*, 2014]. For example, at the Basel Deep Heat Mining Project, *Bachmann et al.* [2012] reported larger Gutenberg-Richter b values near the injection well decreasing with distance. This observation was attributed to pore pressure decay with distance from the well [*Terakawa et al.*, 2012]. The authors suggested that seismic events located near the injection well displayed a broader range of fault orientations hosting mostly smaller events compared to faults activated at larger distances from the injection point. Also, a relation between the largest earthquake magnitude and total injected fluid volume has been observed [*McGarr*, 2014]. The largest events are commonly linked to favorably

oriented faults [e.g., *Deichmann and Giardini*, 2009]. In addition, source-physics simulations of the seismic events from the Basel Deep Heat Mining Project indicate that the maximum earthquake magnitudes may also depend on the orientation of reactivated fault structures and their stress level [*Gischig*, 2015]. Therefore, studying the geometry of preexisting faults and their reactivation during fluid injection and production also has important implications for seismic hazard assessment.

Several approaches have been suggested to quantify the stress state of a fault and how close it is to failure. Particularly, the slip tendency analysis [*Morris et al.*, 1996] quantifies the shear to normal traction ratio of a fault considering its orientation in the stress field and fault friction coefficient. *Moeck et al.* [2009] evaluated the fault reactivation potential using the slip tendency analysis in a geothermal environment. However, the application of the slip tendency analysis requires knowledge on the stress magnitudes. *Sibson* [1985, 1990, 2014] estimated the optimum angle for reactivation of faults with a given coefficient of friction. In these studies, only faults with Andersonian slip (i.e., excluding faults with oblique slip) were considered and thus potential effects of the intermediate stress σ_2 were neglected. *Lund and Slunga* [1999] applied stress tensor inversion and a fault instability concept to identify the actual fault plane from nodal planes of focal mechanisms. Most of these studies did not investigate the potential changes in space and time of the reactivated fault orientations.

In this study, we analyze the reactivation potential of faults inferred from focal mechanisms of induced microseismicity ($M_w < 3.2$) recorded at The Geysers geothermal field, California. We present a relocated seismicity catalog and refined focal mechanisms. The data are inverted to estimate stress field orientation and the fault plane instability coefficients. The instability coefficients are compared with the slip misfit angles from the stress inversion, earthquake magnitudes, b values, spatiotemporal event distribution, and injection rate changes. We discuss our results in the context of the excess pore pressure necessary for fault reactivation. Here we also consider the impact of a temporally varying stress field.

2. Site Characteristics, Seismicity Data, and Hydraulic Parameters

The Geysers geothermal field is one of the largest geothermal fields worldwide in terms of steam production [e.g., *Majer and Peterson*, 2007] and has been in operation for more than 50 years resulting in the occurrence of several hundred thousand induced seismic events [*Majer and Peterson*, 2007] (Figures 1a and 1b). The Geysers is located approximately 100 km north of the San Francisco Bay area. It is also colocated with the San Andreas Fault system that hosts most of the deformation caused by the relative motion of the Pacific and North American tectonic plates. The Geysers field is bound by two regional strike-slip faults, the Maacama and the Collayomi Faults striking NNW-SSE at $\phi_{\mathrm{Mac}} = 332°$ and $\phi_{\mathrm{Col}} = 317°$, respectively, according to the U.S. Geological Survey (USGS) Quaternary Fault Database. The Collayomi Fault is considered to be currently inactive (GPS-derived slip rates are < 1 mm/yr). Slip rates about 13 mm/yr have been derived for the Maacama Fault [*Murray et al.*, 2014], indicating 8% chance of a large earthquake within the next 30 years [*Aagaard et al.*, 2016]. In between them, the geothermal reservoir is crossed by several minor local faults, which have been suggested to have different permeability depending on their orientation [*Jeanne et al.*, 2014a].

The waveform data and *P* wave first-motion polarities used in this study are recorded by the local Berkeley-Geysers (BG) seismic network composed of 31 three-component short period sensors operated at a sampling frequency of 500 Hz. Most sensors forming the network were installed in 2007 and operated successfully for the entire period considered here. Until 2013, the quality of the seismicity waveform database steadily improved but after 2013 the number of manually revised events decreased. This resulted in a reduced number of earthquakes processed and included in the catalog after this time.

We selected a prominent seismicity cluster ($M_w < 3.2$) surrounding the injection wells Prati-9 and Prati-29 in the northwestern part of the field (Figure 1b). The seismic activity from this cluster displays a clear correlation with injection rates [*Martínez-Garzón et al.*, 2013]. The initial seismicity catalog was retrieved from the Northern California Earthquake Datacenter (NCEDC). Between January 2006 and June 2015, a total of 1957 seismic events (M_w 1.4–3.2) has been located within an area of 1×2 km (Figures 1b and 1c). In this part of the field, the steam reservoir extends approximately between 2 and 3 km depth, which is also where most of the seismicity occurs.
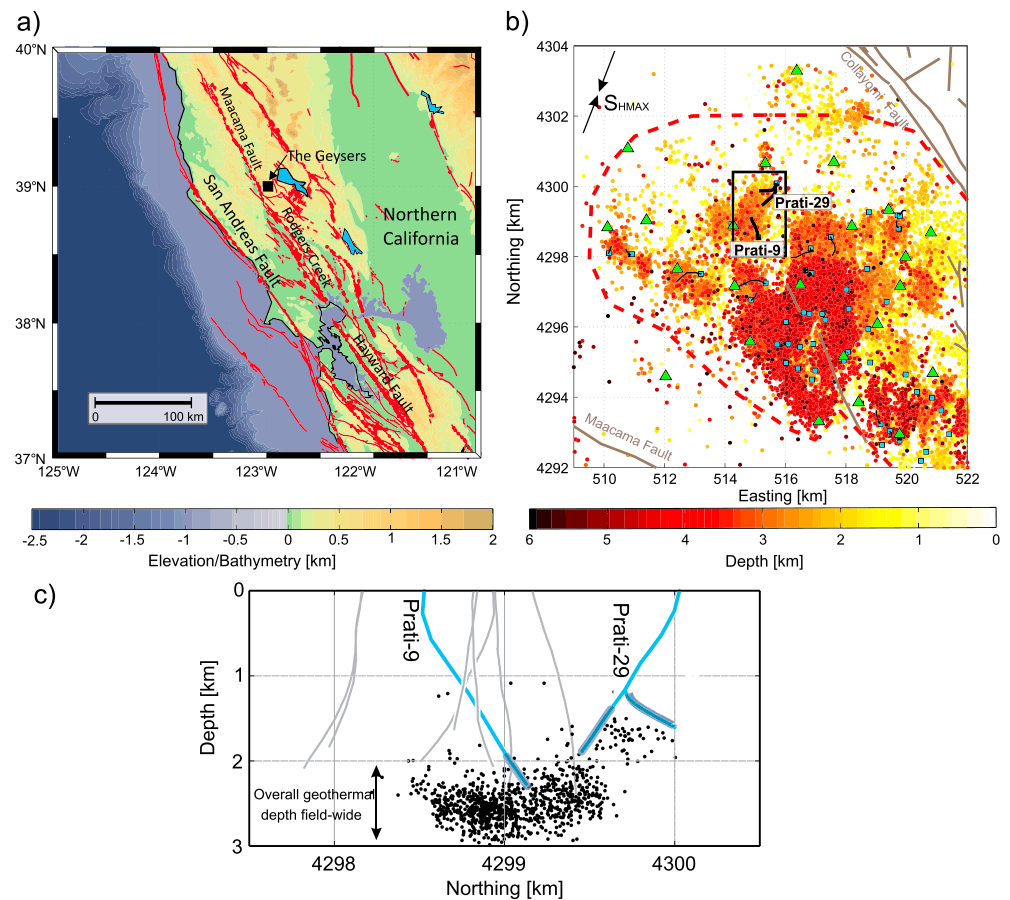
Figure 1. (a) Location of The Geysers geothermal field (black square) with respect to the main quaternary fault structures in Northern California (red traces). (b) Relocated seismicity catalog [*Waldhauser and Schaff*, 2008] from the northwestern The Geysers geothermal field. Green triangles represent position of the local Berkeley-Geysers (BG) seismic stations, respectively. Blue squares and black lines mark the wellhead positions and trajectories of some injection wells throughout the field. Brown lines represent local fault traces. (Quaternary fault database, USGS). (c) Depth section of the relocated seismicity and the injection wells Prati-9 and Prati-29. Grey traces mark the open-hole section of these wells. Light grey lines represent the trajectories of producer wells nearby.

Fluid injection at the well Prati-9 started in November 2007 lasting up to date. A second well nearby, Prati-29, was also used for injection between April 2010 and January 2014. Within this well, two different trajectories were drilled, and possibly, both were used for water injection into the reservoir. Previously, a number of short- and long-term transients in seismomechanical characteristics were identified that are related to changing injection rates. These include distance of seismicity from injection well, different faulting styles, *b* values from Gutenberg-Richter distributions, and stress ratio *R* from stress tensor inversion [*Martínez-Garzón et al.*, 2014; *Kwiatek et al.*, 2015; *Martínez-Garzón et al.*, 2016]. Importantly, the seismicity from this cluster has revealed significant changes of the stress field orientation of approximately ≈ 15–20° during periods of high injection rates [*Martínez-Garzón et al.*, 2013]. Since the beginning of injection operations at these wells, the fluid volume in the reservoir increased with time suggesting a slow increase of reservoir pore fluid pressure. Five nearby production wells operate since 2011, but no correlation between steam production and seismic activity has been observed [*Kwiatek et al.*, 2015].

3. Methodology

3.1. Refinement of Hypocenter and Focal Mechanism Catalog

We refined the seismicity catalog by applying the double-difference relocation software Hypo-DD [*Waldhauser and Ellsworth*, 2000] using manually refined picks. This improved the relative precision of hypocenter

locations to about ±40 m (68% confidence interval). The refined relocation catalog contains 957 seismic events, i.e., ~50% of the initial catalog. A comparison between initial and relocated hypocenter catalogs is provided in Figure S1 in the supporting information.

To derive the best possible quality of focal mechanisms, we applied the following selection criteria to the input data:

1. We only used phases from the local Berkeley-Geysers (BG) network to provide consistent network characteristics (e.g., sensor orientation).
2. We used only signals with quality weights 0 (most impulsive polarities) or 1 in an attempt to exclude wrong P wave polarities to the most possible extent.
3. We included only seismicity with a takeoff angle gap of <60° (from polarities with weights 0 and 1) and an azimuthal gap of <90°.

The Geysers geothermal field and the local seismic network BG cover an area of about 20 km × 20 km. The approximate minimum and maximum epicentral distances between earthquake sources and stations are 0.3 km and 16.2 km, respectively. Therefore, a substantial part of phase data represents direct P wave arrivals providing a good coverage of the focal sphere. In total, 588 focal mechanisms were in agreement with the imposed selection criteria.

Focal mechanisms were recalculated based on the new hypocenter locations using the HASH software [*Hardebeck and Shearer*, 2002] inverting first-motion polarities for constrained double-couple focal mechanisms. The ray tracing parameters were calculated using a 1-D velocity model [*Eberhart-Phillips and Oppenheimer*, 1984]. We allowed for ±2° and ±3° uncertainties in the source-receiver azimuth and takeoff angle, respectively, based on the observed differences between takeoff angle estimates using different velocity models available. For each focal mechanism, HASH calculates all the acceptable solutions assuming an allowed polarity misfit. Then, the software calculates the average of the acceptable solutions and the angles γ between each acceptable solution and the average. Next, HASH removes iteratively all the solutions forming larger angles γ than a predefined threshold (cutoff angle, here set to 30°). Finally, HASH calculates the "best" focal mechanism as the average of the remaining acceptable focal mechanisms [see *Hardebeck and Shearer*, 2002].

Different input options such as including stations at regional distances and including different quality weights were tested to check the sensitivity of the results. We observed that including first-motion polarities of events with best weights from all regional stations or, alternatively, including polarities with best weights of events within a radius of 50 km resulted in an increased number of phases per event. However, this also resulted in a substantial increase in the number of misfit polarities per focal mechanism. Therefore, only polarity data from local stations were considered.

Lastly, we further constrained the selection of focal mechanisms to fault plane angular errors <20°, where the fault plane angular error is defined as the RMS angular difference between all acceptable focal mechanisms for an event and the average solution. This is a comparable or smaller error than of other high-quality focal mechanism catalogs estimated with HASH (e.g., the Southern California catalog, where the best quality ranking was considered <25°) [*Yang et al.*, 2012]. The procedure resulted in 304 high-quality fault plane solutions out of the original 1957 seismic events.

3.2. Stress Tensor and Fault Instability

Stress tensor inversion of the 304 high-quality focal mechanisms resolves the orientation of the three principal stresses $\sigma_1, \sigma_2, \sigma_3$ and a stress ratio (also called relative stress magnitude R) defined as follows:

$$R = \frac{\sigma_1 - \sigma_2}{\sigma_1 - \sigma_3} \tag{1}$$

The stress tensor inversion requires the strike, dip, and rake of the fault planes as input data. In some cases, slickensides may be available from geological data [e.g., *Michael*, 1984] but commonly earthquake focal mechanisms are inverted. Without additional information, it is not possible to identify the true fault plane and the auxiliary plane from a focal mechanism. Fault plane ambiguity does not significantly affect the estimated stress tensor orientation, but it does affect the stress ratio R [*Vavryčuk*, 2015]. In the linear inversion procedure developed by *Michael* [1984, 1987] one of the two nodal planes is selected randomly to represent the fault plane. An alternative approach is to select the planes with the smallest slip misfit β between observed slip

and shear traction vectors [e.g., *Terakawa et al.*, 2012]. Finally, a third approach is to use a Mohr-Coulomb failure criterion to select the most unstable fault plane orientations in a given stress field [e.g., *Lund and Slunga*, 1999].

We applied the iterative method STRESSINVERSE [*Vavryčuk*, 2014] using available focal mechanisms to invert for the stress field orientation and stress ratio R. A linear stress tensor inversion is first performed selecting randomly one of the two nodal planes that represent possible fault planes in each focal mechanism. To estimate the true fault plane, a fault instability coefficient [*Vavryčuk*, 2011; *Vavryčuk et al.*, 2013] is calculated:

$$I = \frac{\tau + (1 - \sigma_n)}{\mu + \sqrt{1 + \mu^2}}$$

(2)

where τ and σ_n are shear and normal traction vectors calculated from directional cosines and the stress ratio R and μ is the fault friction coefficient (note that compression is taken positive). Fault instability I quantifies how close the orientation of a fault is to that of the optimally oriented fault given an assumed stress field orientation and a friction coefficient. Since the stress tensor inversion does not provide absolute stress magnitudes, *Vavryčuk et al.* [2013] used normalized stress magnitudes to estimate instability. This is in contrast, for example, to the slip tendency analysis that requires absolute stress values. Thus, instability defined in equation (2) assesses the "relative" stability of the fault with respect to the stress field orientation. The parameter I is in principle independent of the pore pressure or the cohesion of the rock [*Vavryčuk et al.*, 2013]. However, its efficiency in picking the correct fault plane was observed to decrease at high pore pressure levels [*Martínez-Garzón et al.*, 2016]. Fault instability varies from $I = 0$ for the most stable faults to $I = 1$ for faults oriented optimally for failure.

Using an iterative procedure, instability I is calculated for both nodal planes of a focal mechanism and the nodal plane with higher I is selected for the next iteration of the stress tensor inversion (no focal mechanisms are rejected in this process). The approach also allows for a concurrent search for the friction coefficient maximizing instability of all fault planes [*Vavryčuk*, 2014]. Finally, the uncertainty of the stress tensor orientation is derived following Michael's approach by performing bootstrap resampling (500 iterations) of the original data set. In each bootstrap resampling, a population of fault planes is selected randomly from the two nodal planes of each focal mechanism [*Michael*, 1987].

The determination of focal mechanisms and stress tensor inversion both introduce errors that can affect fault instability estimates. In an attempt to statistically account for the combined errors of focal mechanism determination and stress tensor inversion, we first calculate the instability coefficient distribution using each focal mechanism and the uncertainties in the stress tensor orientation and stress ratio after 500 bootstrap resampling runs (Figure 2a). The obtained instabilities are found to follow a unimodal distribution. In a similar approach, we calculate the instability distribution using the best stress tensor orientation and the uncertainties in the focal mechanisms from the (maximum) 300 acceptable mechanisms (Figure 2b). In this case, the obtained distributions are also unimodal.

Finally, we combine the uncertainty of the stress tensor inversion from bootstrap resampling with the uncertainty from the acceptable focal mechanisms. To do so, we perform 2000 resampling runs for each event. For each iteration we selected a random stress tensor from the bootstrap resampling and a fault plane solution from the acceptable fault planes. This procedure resulted in a sample of 2000 normal and shear traction vectors and instabilities (Figure 2c). The most likely instability coefficient for each earthquake (I^{likely} in Figures 2c and 2d) was calculated by finding the mode of a two-dimensional probability density function in normal traction σ_n—shear traction τ space. To evaluate the uncertainty of the instability coefficients using a single confidence interval, we calculated the 15% and 85% quantiles of the instability distribution (Figure 2d). In the following, only most likely instabilities are used and they are referred as I.

In addition, we also calculated the slip misfit angle β for all focal mechanism nodal planes. However, *Lund and Slunga* [1999] suggested that in constraining true fault planes from focal mechanisms, fault instability provided better results compared to minimizing slip misfit angles. *Lund and Slunga* [1999] used synthetic tests including realistic noise levels as well as real data. Combining both approaches allows for effective use of all available information on the focal mechanisms toward evaluating the fault reactivation potential.

3.3. Effect of Time-Dependent Changes in Stress Field Orientation

By inverting the entire data set, a homogeneous stress field is assumed. However, the stress field within the seismicity cluster studied here has been observed to vary in time in accordance with changes in flow rate
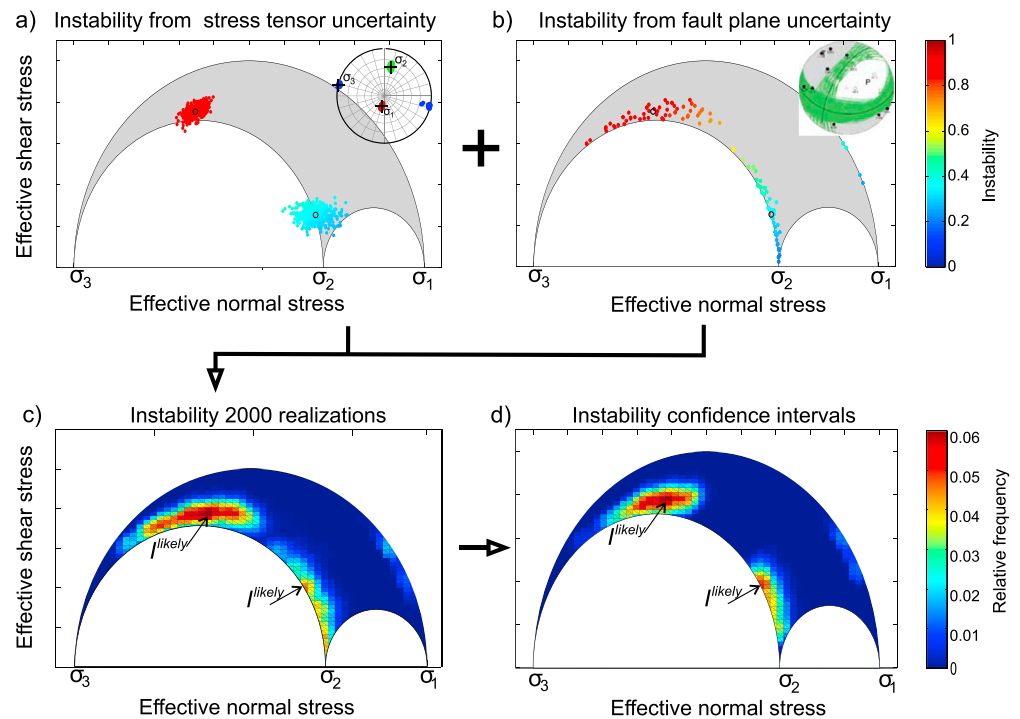
Figure 2. (a, b) Instability uncertainty distributions (colored points) corresponding to the best fitting instabilities of two seismic events (black circles) represented in the Mohr diagram and estimated from the uncertainties of stress tensor orientation and focal mechanism. Top right of Figure 2a shows the bootstrap resampling distribution of the stress tensor orientation in the stereonet. Top right of Figure 2b shows an example of the acceptable fault plane solutions (green lines) used to define uncertainty of a focal mechanism. (c) Probability density function of the instabilities of the same two events after performing 2000 sampling runs. (d) Probability density function of the final uncertainties related to two seismic events after removing the lowest and highest 15% of values. I^{likely} represents the most likely instability (see text for details). For definition of Mohr circles see, e.g., *Jaeger and Cook* [1971].

[e.g., *Martínez-Garzón et al.*, 2013]. To investigate the effect of assuming a constant far-field stress orientation on the inversion results, in section 5.1 we apply a time-dependent nodal plane selection process as for STRESSINVERSE and implement it to the SATSI [*Hardebeck and Michael*, 2006] and MSATSI stress inversion software [*Martínez-Garzón et al.*, 2014]. The SATSI stress inversion procedure is designed to resolve temporal or spatial changes in the stress field orientation by applying a linear damped stress tensor inversion. By choosing the damping parameter to minimize the data variance and the model length, physical changes in the stress field are maintained while artificial sources of error are smoothed out. Here we first applied a linear stress inversion separately for each time window to find the best stress field orientation without the use of damping parameter. Then, we select the fault plane with maximum I for the estimated stress field orientation and the stress tensor inversion is performed again using an iterative process. Once the fault planes are optimized, we apply the damped inversion as in SATSI.

4. Results

4.1. Instability and Slip Misfit Angle of Reactivated Fault Planes

The 304 high-quality fault plane solutions with fault plane error $< 20°$ are included in a single stress tensor inversion assuming a homogeneous stress field (to test this hypothesis, see section 5.1). The results reveal an oblique normal faulting regime with the principal stress axes σ_1 (193° north over east, 64.5° measured from horizontal), σ_2 (13°, 25°), and σ_3 (283°, 1°), respectively, and a stress ratio of $R = 0.29$. In addition, the stress tensor inversion indicates for each event the fault plane with the highest instability, the instability coefficients, the slip misfit angle β, and an optimum friction coefficient $\mu = 0.5$ for the whole set of inverted faults. Subsequently, we statistically estimate the most likely instabilities I (Figure 3a). These parameters for each event are provided in Table S1.
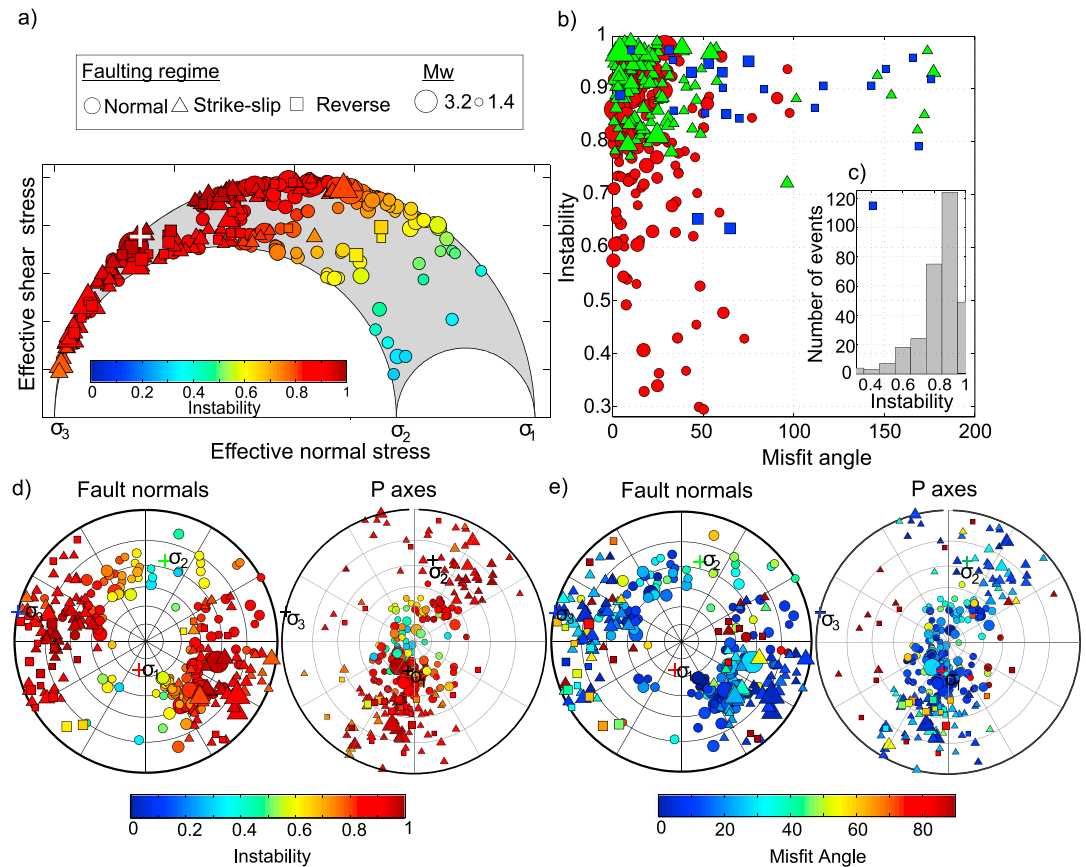
Figure 3. (a) Fault planes projected on the Mohr diagram color encoded with the estimated instability coefficients *I* (see text for details). White cross shows the location of the optimally oriented fault. (b) Relation between fault instability *I* and slip misfit angle β. Color is encoded with faulting type, where red represents normal faulting, green represents strike-slip faulting, and blue denotes reverse faulting. (c) Histogram of number of events and corresponding instabilities. (d) Stress field orientation, fault normals, and *P* axes of the focal mechanisms plotted in the lower hemisphere stereonet, color encoded with *I*. (e) Stress field orientation, fault normal, and *P* axes of the focal mechanisms color encoded with β. In Figures 2a, 2b, 2d, and 2e symbol size is encoded with magnitude and marker type represents faulting regime.

The complete stress state cannot be characterized from the stress tensor inversion. Therefore, a normalized Mohr circle is used for representation of the results. About 71% of the 304 fault planes show instability coefficients $I > 0.8$ indicating that these faults were favorably oriented for failure (Figures 3a and 3c). This suggests that small stress perturbations may result in reactivation of favorably oriented faults producing substantial seismicity [*Zoback*, 2007]. Interestingly, 25% of events occurred on faults with lower instabilities ($0.5 \leq I \leq 0.8$) including 3% of events with very low instability $I < 0.5$. These seismic events reflect reactivation of misoriented fault planes, which may be explained either by lower friction coefficients or by local stress perturbations, e.g., related to fault structure and segmentation, pore pressure, or temperature changes. The *P* axes of events characterized by low instabilities frequently show plunges close to 90° corresponding to normal faulting regime (Figure 3d).

The slip misfit angle β is defined as the angle between observed slip direction along a fault plane and the orientation of the shear traction vector inferred from stress tensor inversion. The median misfit angle from the set of 304 focal mechanisms is $\beta = 19.5°$. This is in agreement with the average slip misfit angle of up to 20° considered in *Michael* [1991] to represent a homogeneous stress field. We observe a small population of faults with low instability and also relatively low misfit angles ($\beta \leq 50°$), displaying slip directions that match the stress field. In addition, a second small population is favorably oriented ($I > 0.8$) but these faults are observed to have significantly larger misfit angles (Figures 3b and 3e). The largest slip misfit angles β are found for faults with *P* axes not contained in the plane defined by the σ_1 and σ_2 directions (Figure 3e). The
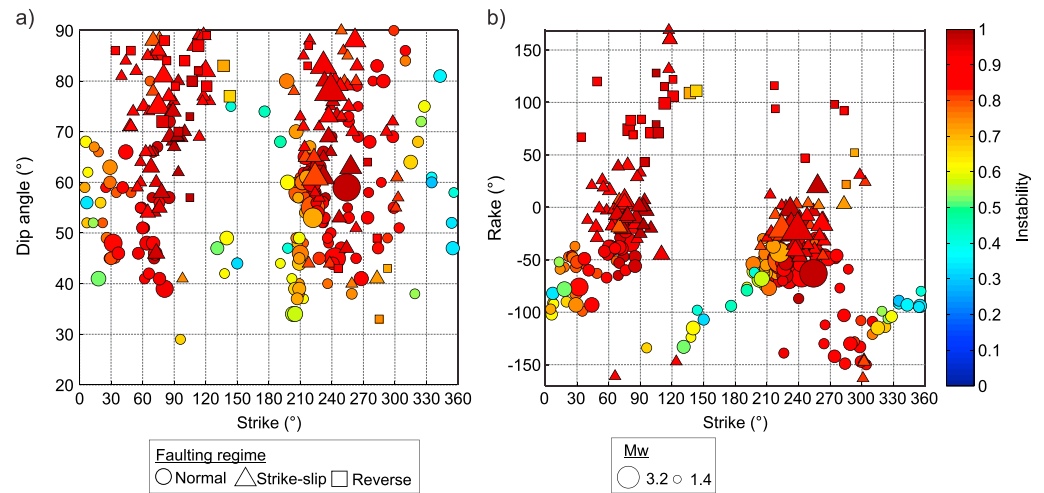
Figure 4. Characterization of fault geometries. (a) Strike ϕ and dip angles δ. (b) Strike ϕ and rake λ angles. Color, size, and symbol represent fault instability, moment magnitude, and faulting style, respectively.

relation between fault instability and the slip misfit angles shows a general cloud of points clustering around high values of instability and low values of misfit, but outlying populations with large slip misfit angles and large instability and vice versa are also observed (Figure 3b). It is conceivable that focal mechanisms with large slip misfit angles may not be well represented by the obtained stress field orientation that represents an average for the crustal volume populated by the seismicity cluster. Therefore, we further check how is the instability distribution modified if only the 251 focal mechanisms with $\beta \leq 45°$ are considered. Out of these focal mechanisms, 73% display $I \geq 0.8$, 23% are observed to have instabilities between $0.5 \leq I \leq 0.8$, and 3% contain $I < 0.5$. Therefore, the statistics are very similar regardless of whether these events are included or not.

4.2. Fault Geometry and Instability

We analyze how the instability coefficient varies with respect to the geometry of the fault plane described by strike $\phi[0, 360°]$, dip $\delta[0, 90°]$, and rake $\lambda[-180°, 180°]$ following the convention of *Aki and Richards* [2002]. The respective faulting regime (i.e., normal, reverse, and strike slip) is based on which of the *P, T* and *B* axes is closest to vertical.

Normal faulting events represent the largest group and are observed to have fault instabilities distributed over the whole range of I [0.3, 1] (circles in Figure 3). Strike-slip mechanisms are found mostly on favorably oriented faults with $I \geq 0.8$ (triangles in Figure 3). The majority of seismic events indicate oblique faulting with dominantly normal or strike-slip kinematics. Fault rake values vary between $\lambda = -90°$ and $\lambda = 10°$ (Figure 4b).

In general, the relation between fault instability I and fault strike ϕ and dip angle δ depends on the stress tensor. For this data set, fault strike dominates instability and the dip angle has a relatively smaller effect. Often, lower instabilities were observed for shallower dipping fault planes (Figure 4a). Focal mechanisms show a dominant fault orientation striking approximately $\phi = 60°$ with dip angles between $\delta = 30° - 70°$ for normal faulting events. For strike-slip mechanisms typically dip angles $\delta > 70°$ are observed. This is in good agreement with the fault plane orientations estimated by *Boyle and Zoback* [2011, 2014]. Interestingly, some faults with low-instability I cluster around $\phi = 350°$ (Figure 4). Activation of these faults resulted in seismic events with a fault rake of $\lambda = -90°$, representing pure normal faulting.

However, we also observed few reverse faulting events that cluster around $\phi = 100°$ and display steep dips of $\delta > 70°$ representing nearly vertical faults with rake $\lambda \approx 100°$ (Figure 4b). These events occur on favorably oriented faults with high instabilities covering the magnitude range M_w [1.3, 2.3] (squares in Figure 3). The slip misfit angles of these events are large with $\beta > 90°$. This clearly suggests that the a priori assumption of a homogenous stress field does not always hold and that local stress heterogeneities do exist (Figures 3c, 3d, and S2).
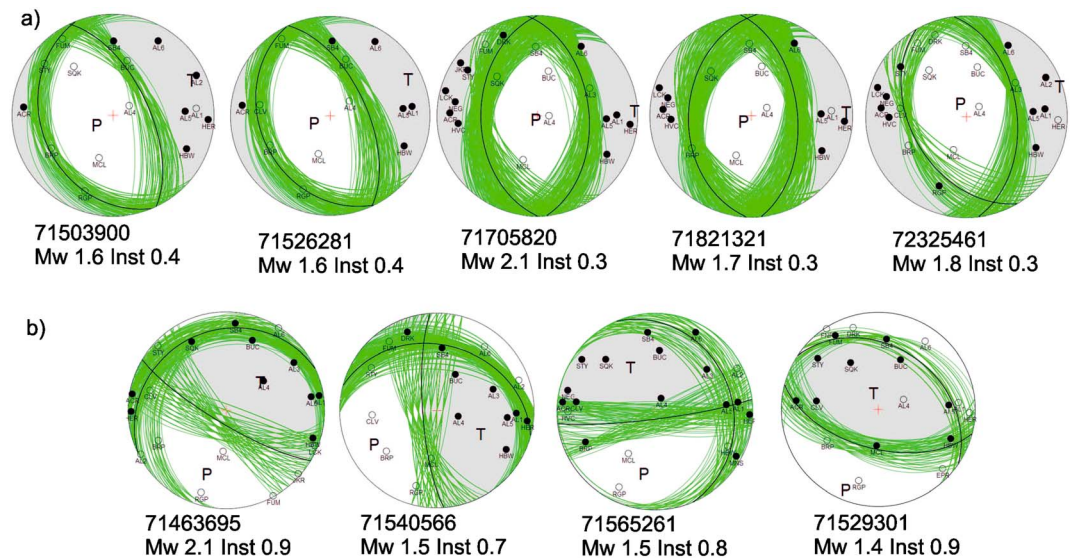
Figure 5. Examples of focal mechanisms calculated with HASH [*Hardebeck and Shearer*, 2002]. Green lines represent acceptable fault planes within a specified cutoff angle (here 30°). Black and white dots represent the location of the used stations with positive and negative polarities, respectively. (a) Examples of low-instability mechanisms, where the most unstable plane is oriented with strike direction $\phi \approx 355°$. (b) Examples from obtained reverse faulting events.

We manually reevaluated waveforms and fault plane solutions of events with low instabilities or high slip misfit angles (Figure 5a). These focal mechanisms are well constrained with at least 15 high-quality polarity readings, appropriate azimuthal and takeoff angle coverage, and a polarity misfit of about 1 per event. The waveforms and polarities of the reported reverse mechanisms with large misfit angles are mostly well constrained with ~45% of the events containing most of their acceptable solutions as reverse faulting (Figure 5b).

Fault plane solutions for 75% of the events are constrained by at least 18 high-quality first-motion polarities (Figure 6a). Fault planes with larger instabilities ($I \geq 0.8$) contain fault plane angular errors as low as 5°, but faults covering the full range of errors are observed (Figure 6b). However, fault planes with $I \leq 0.6$ usually have fault plane angular errors $> 9°$ suggesting slightly larger errors for less favorably oriented faults. No clear
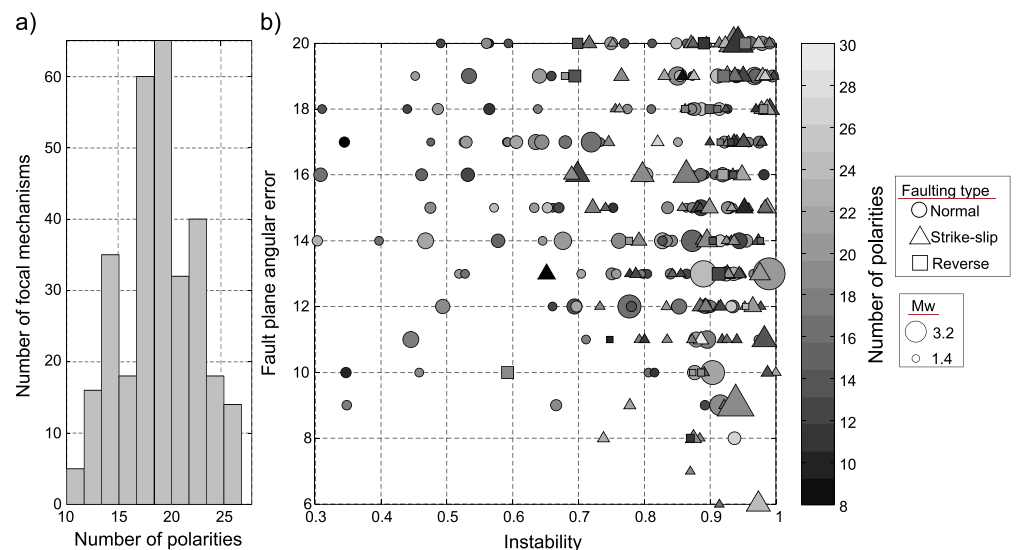

Figure 6. (a) Number of focal mechanisms characterized by a certain number of high-quality polarities. (b) Distributions of angular fault plane error (in degrees) with respect to fault instability.
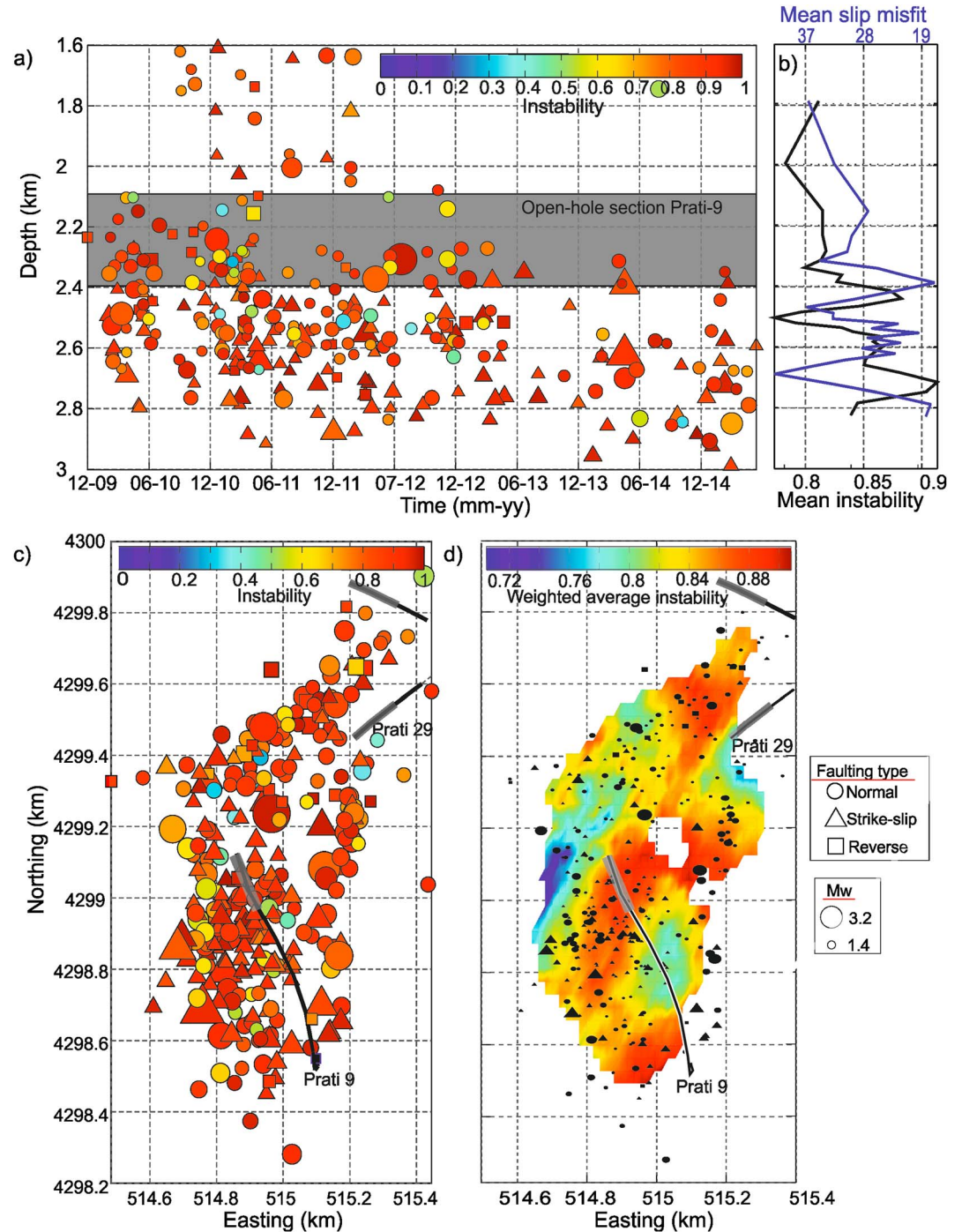
Figure 7. (a) Depth distribution of the seismicity with time. Grey semitransparent area corresponds to the open-hole section of well Prati-9. (b) Mean instability and slip misfit angle as a function of depth. (c) Distribution of the seismicity in map view. (d) Weighted average of instabilities using seismic events within a radius of 125 m (note the different color scales). Weighting is set as $z - \sum \sqrt{\frac{I}{R}} / \sum \sqrt{\frac{1}{R}}$, where I is the fault plane instability of the events and R the distance between the event and considered point. In Figures 7c and 7d, grey semitransparent intervals show open-hole sections of the wells.
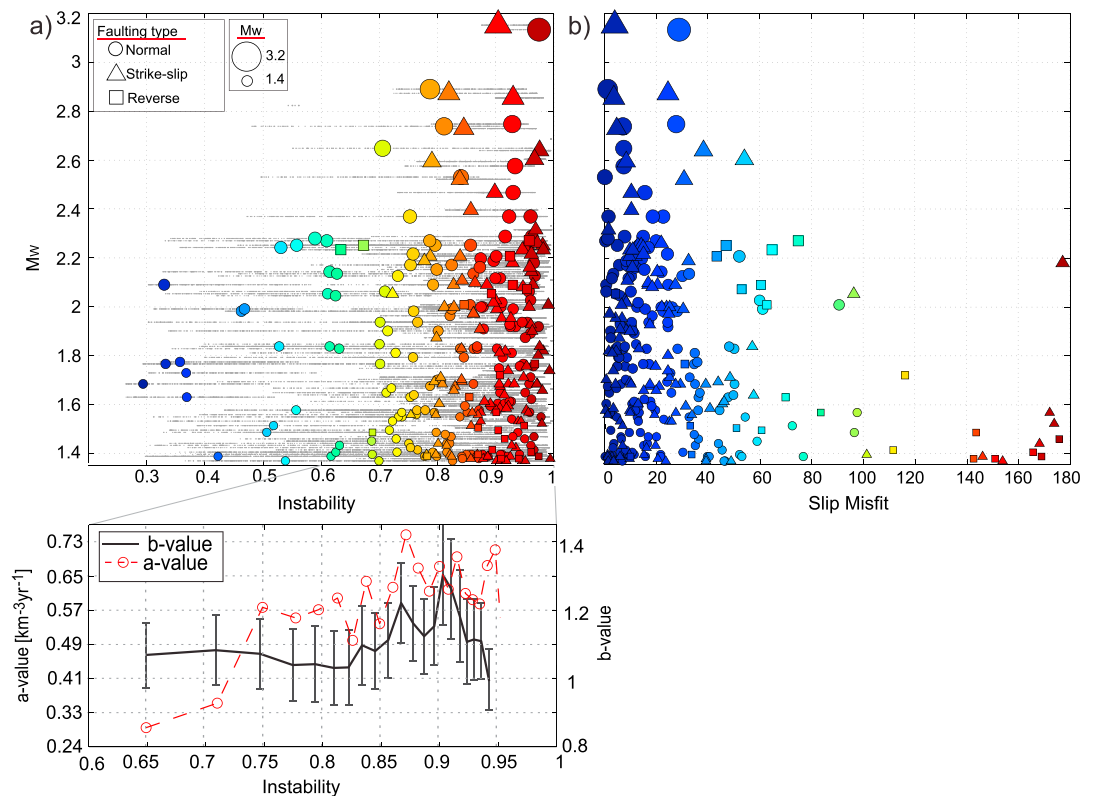
Figure 8. (a) Moment magnitude as a function of most likely fault instability I. Colored symbols represent most likely instabilities, where color, symbol, and size represent instability, faulting style, and magnitude, respectively. Small grey points forming horizontal lines represent instability uncertainties. (b) Moment magnitude as a function of slip misfit. Color is encoded with slip misfit, and size and symbol show the same as in Figure 8a. (c) a (red discontinuous line) and b values (black solid line) from the Gutenberg-Richter distribution. Black vertical bars show b value confidence interval.

dependency of number of polarities used to estimate the mechanisms and angular error is observed. Comparable fault plane error distributions are found for normal and strike-slip faulting regimes. Events indicating reverse faulting have average angular errors >16°.

4.3. Spatial, Temporal, and Magnitude Distributions of Fault Instability and Slip Misfit Angle

Most of the seismicity at faults with low instability ($I \leq 0.4$) is located at 2.1–2.7 km depth, thus occurring around or below the open-hole section of the Prati-9 well (Figure 7a). Some events with instabilities $0.5 \leq I \leq 0.7$ are distributed at shallower depths, which suggests that they may occur in relation to the second well Prati-29, whose open-hole section extends from 1.5 km to 1.9 km depth. Below 2.6 km, a substantial amount of seismicity displays strike-slip mechanisms reactivating favorably oriented faults ($I \geq 0.8$).

We find two regions with average lower instability with $I < 0.8$ (Figure 7b) at 2 km and 2.5 km depth (below the open-hole section of the injection wells). The same regions are found to have larger mean misfit angles. The distribution of mean instabilities and slip misfit angles versus hypocenter depths is based on moving windows of 20 events. At 2.7 km depth, fault instabilities show a maximum with $I = 0.9$ and also a maximum in slip misfit, suggesting that in the deepest part of the reservoir mostly favorably oriented faults have been activated. However, they mostly rupture in strike-slip and reverse faulting, indicating that some may have remarkably large slip misfit angles. Below the open-hole section of well Prati-9, the instabilities I decrease rapidly. At this depth, pressure perturbations due to fluid injection are larger. Down to approximately 2.6 km the mean slip misfit is anticorrelated with the mean fault instability. Below the open-hole section of the wells, lower instabilities are observed together with increased misfit angles. Box plots of the distribution of instability and slip misfits with depth are provided in Figure S3.

In map view the analyzed seismicity cluster shows an elongated maximum of instabilities with $I \geq 0.86$ that is roughly aligned with the trend of σ_1 and σ_2 (Figures 7c and 7d). Most of the low-instability events occurred

within a lateral distance < 600 m to the well Prati-9. However, directly below the open-hole section, the average instability is comparatively larger. Since pore pressure changes are the largest near the open-hole section of the well, there is a higher probability to activate faults with a broader range of orientations and also to promote local stress changes which may modify the slip orientation of the faults. A relatively large number of seismic events with varying fault orientations were also observed around the injection depth (>500 m) at the Basel Deep Heat Mining project [*Bachmann et al.*, 2012; *Terakawa et al.*, 2012]. Also in our study, most of the seismicity occurs within a few hundred meters distance from the well.

Lastly, for high I or low β there is a broader range of magnitudes observed (including the largest magnitudes in the data set), whereas a narrower magnitude range covering lower magnitudes is visible for lower I or high β (cf. Figures 3, 4, and 8). The two largest events (M_w 3.2) occurred on fault planes with high instabilities $I \geq 0.9$ and slip misfit angles $\beta < 40°$ (Figure 8a). Both events occurred on faults that were almost in optimal orientation for failure within the resolved stress field.

We calculate the dependence of the a and b values of the Gutenberg Richter relation with the fault instability using a goodness-of-fit method [*Woessner and Wiemer*, 2005]. The events are sorted according to their fault instability for moving windows of 70 events. The obtained b values (black line in Figure 8c) remain approximately constant, and they tend to slightly increase with increasing I. A sharp decrease is visible for faults close to optimal orientations. However, the estimation of the most likely instabilities may have also affected the boundaries of the distribution. The a value as a quantitative measure of the earthquake activity is also observed to increase for favorably oriented faults. These faults host ~72% of the total seismicity (Figures 8a–8c).

5. Discussion

Fluid-induced seismic events in the northwestern part of The Geysers geothermal field show a large variety in faulting mechanisms implying a broad range of reactivated fault orientations. A central assumption in stress tensor inversion is that the stress field is homogeneous in the studied region [*Gephart and Forsyth*, 1984] and that the range of focal mechanisms used for the inversion may be attributed to a unique stress tensor. *Hardebeck and Hauksson* [2001] suggest that reliable inversion results are expected for a RMS angular difference of the mean fault mechanism of $> 30°–45°$ depending on noise and data quality. To assess the agreement between an observed fault with respect to the inverted stress field, the misfit angle between observed slip vector and predicted shear traction on that plane was determined [e.g., *Michael*, 1991]. However, the large misfit angles and low fault instability coefficients observed here indicate that locally some stress field heterogeneities may be present. Local stress heterogeneities may be caused, for example, by complex fault structures, pore pressure variations, and changes in lithology. Stress heterogeneity has also been found from borehole breakouts at shallow depths (~3–5 km) [*Hickman and Zoback*, 2004].

Although we have assumed a homogenous stress field, stress inversion from induced seismicity at The Geysers and other geothermal reservoirs often shows significant stress variation with depth typically changing from normal to strike slip [*Cuenot et al.*, 2006; *Martínez-Garzón et al.*, 2013]. *Martínez-Garzón et al.* [2013, 2014] show that both stress field orientation and geometry of reactivated faults vary in time and with depth in response to short-term fluid pressure changes. This indicates that reservoir faults and fractures activated during stimulation are subjected to varying stress states ranging from stable to critical. Therefore, the impact of a time-varying stress field on these results needs to be evaluated in more detail. We address the influence of temporal variations in the stress field in section 5.1.

The 304 seismic events with M_w [1.4–3.2] studied here occurred near the injection wells Prati-9 and Prati-29. Most of the reactivated faults have strike and dip angles favorably oriented for failure in the local stress field and thus display high fault instability coefficient I, although many of them slipped in a nonoptimal orientation with large misfit angle β. Interestingly, some fault planes with rather low instabilities were also reactivated with low misfit angles irrespective of their unfavorable orientation. These low-instability events are observed to occur in the lower part of the open-hole section of the wells and also just below the bottom of the well, where the largest injection-related pressure changes are expected (Figure 7a). In contrast, in the deepest portion of the seismicity cluster, only faults with almost optimal orientation are reactivated, but many of them display larger slip misfit angles.
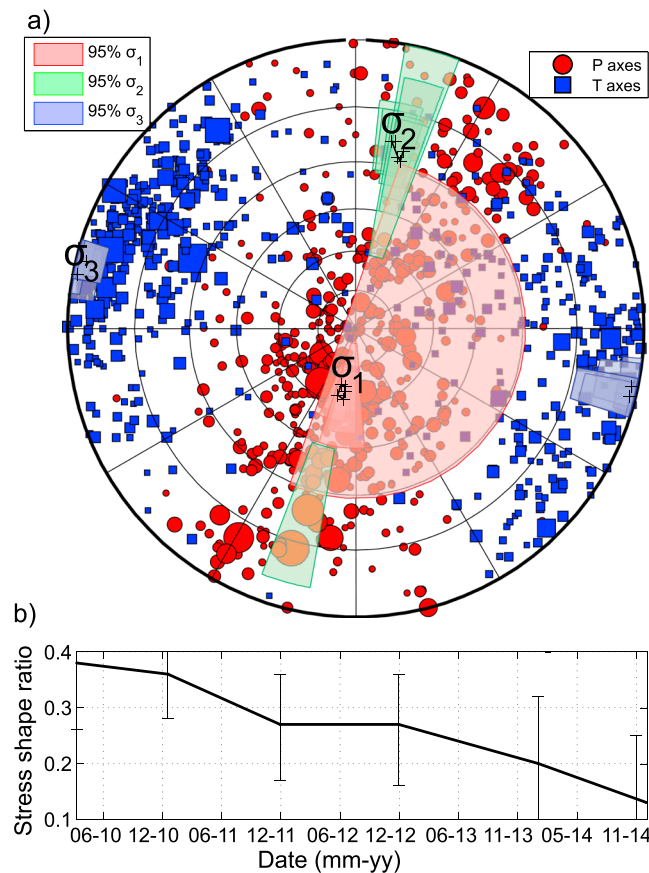
Figure 9. Evolution of stress field orientation from 2010 to 2015. (a) Stress tensor orientations every 6 months plotted in lower hemisphere projection. Crosses represent best solutions from each inversion. Red and blue symbols show the *P* and *T* axes distribution, respectively, with earthquake magnitude size encoded. (b) Corresponding variations of the stress ratio *R* for the analyzed time period. Vertical bars represent 95% confidence intervals.

In addition, large magnitude events are observed to preferentially occur at faults displaying higher *I*. However, the seismic productivity (*a* value) along these faults is also high. Therefore, we perform a statistical test to assess how the varying productivity affects the occurrence of large magnitude events at low and high instabilities (supporting information Text S1 and Figure S5). The first test confirms the relatively larger number of large magnitude events at high instabilities than expected from the magnitude-frequency distribution from the smaller events. However, in the second test the lack of large magnitude events observed at low instabilities may be purely a result of low productivity. Frequent ruptures along favorable orientations are expected to decrease fault complexity possibly modifying the frictional strength of these faults [*Amitrano*, 2003]. It is thus conceivable that increasing fault damage and crack density may promote the occurrence of larger magnitude events along favorably oriented faults. These findings are in agreement with recent source simulations indicating that the largest events related to pore pressure perturbations occur o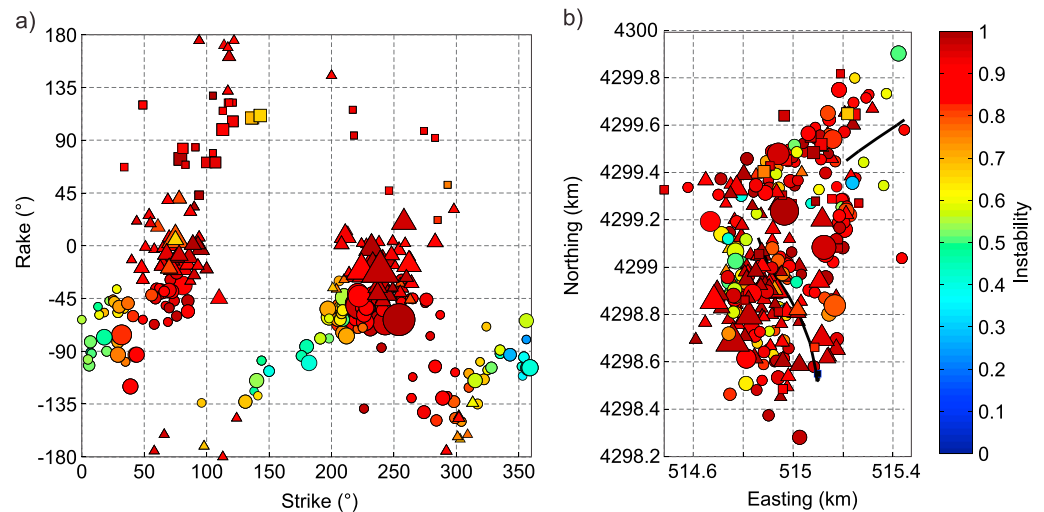n critically stressed faults with optimal orientations, where ruptures may propagate beyond the pore pressure front [*Gischig*, 2015]. Also, critically stressed fault planes activated at the Basel Deep Heat Mining project were found hosting the largest seismic events [*Terakawa et al.*, 2012]. In addition, on favorably oriented strike-slip faults worldwide, events occur with larger observed maximum magnitudes compared to other less favorably oriented strike-slip faults with comparable fault lengths [*Martínez-Garzón et al.*, 2015].

5.1. Effect of Changing Stress Field on Fault Reactivation

At the selected location at The Geysers geothermal field, local stresses were found to change, mainly related to fluid injection, which directly affects thermal stresses and pore fluid pressure in the reservoir. On a longer time scale, the stress ratio *R* was observed to slightly decrease [*Kwiatek et al.*, 2015; *Martínez-Garzón et al.*, 2016]. Within shorter time periods, *Martínez-Garzón et al.* [2013] described a rotation of principal stresses up to 15°–20° during high-rate fluid injections. In this section we analyze how these stress variations may affect our results.

To evaluate the potential effects from a long-term changing stress field, we inverted the 304 high-quality focal mechanisms dividing them into time periods of 6 months between June 2010 and June 2015. We then applied the updated MSATSI method incorporating the selection of fault planes with the highest instability from each focal mechanism. The number of events included in each inversion varies between 45 and 185 events. During the selected 5 years the stress field orientation has maintained approximately normal faulting and no significant long-term changes in orientation are observed (Figure 9a). The stress ratio decreased from $R = 0.38$ in 2010 to $R = 0.13$ in 2015. Since shear and normal tractions depend on

Figure 10. Instability of fault planes derived using a time-varying stress field orientation. (a) Fault rake λ as a function of fault strike ϕ. (b) Map view of the seismicity. For Figures 10a and 10b, color, size, and symbol represent instability, magnitude, and faulting style, respectively.

the stress ratio R, a lower stress ratio would result in slightly reduced instabilities. However, these variations are rather minor [*Xu et al.*, 2010].

To assess the effect of episodic stress rotations, we inverted the focal mechanisms using a moving time window containing 20 seismic events. The small time windows increased the temporal resolution at the cost of potentially increasing error in stress tensor orientation. We find no significant differences in the instability distributions compared to those derived from the time-constant stress tensor orientation (cf. Figures 4b, 7b, and 10a). The orientation of reactivated faults is approximately preserved, while the low-instability faults tend to cluster more than before (Figure 10b). Furthermore, the average slip misfit angle is not significantly reduced by inverting smaller focal mechanism subsets and the median misfit angle remains at 20°.

5.2. Perturbation of Fluid Pressures and Thermal Stresses

Increase of the reservoir fluid pressure due to high injection rates will reduce effective stresses and shift the stress state on a fault closer to failure. Depending on the fault orientation, the change in fluid pressure required to initiate failure varies, with the largest increase in fluid pressure needed for failure of low-instability faults. Therefore, the instability coefficient also provides constraints on the pore fluid pressure change required to initiate failure, similar to the overpressure coefficient from *Terakawa et al.* [2012]. High injection rates lead to elevated pore pressures in the vicinity of the injection wells that will propagate and decay in amplitude away from the well governed by hydraulic diffusion [*Shapiro et al.*, 2003]. The reservoir pore pressure changes from stimulation at the northwestern Geysers have been estimated to be in the range of 1–10 MPa based on thermohydromechanical modeling [*Rutqvist et al.*, 2013; *Jeanne et al.*, 2014a, 2014b] and injectivity-test logs [*Martínez-Garzón et al.*, 2014]. The reservoir stresses are also affected by the injection of cool water (~70°) into a hot reservoir rock (>240°C) potentially leading to fractures due to the thermal contrast between the fluid and the host rock. The thermal stresses were estimated to reach 26 MPa at the wellbore wall, but they are expected to decrease rapidly with distance [*Martínez-Garzón et al.*, 2014].

In the following, we estimate the shear and normal stresses acting on faults and the pore pressures necessary to reactivate fault planes with different instabilities I using the pore pressure tomography technique [*Terakawa et al.*, 2012, 2013; *Terakawa*, 2014]. For this we only selected the 251 focal mechanisms with slip misfit angles $\beta < 45°$ to ensure that all events are in good agreement with the inverted stress field. To estimate stress magnitudes, we assume that the vertical stress S_V at the hypocenter location of each event is given by the weight of the overburden (lithostatic pressure). We use a rock density of $\rho = 2700\,^{kg}/_{m^3}$. Then, S_1 is obtained by projecting S_V along the S_1 direction obtained in this study. We assume that the minimum compressive stress S_3 may be estimated from the frictional strength of faults assuming a friction
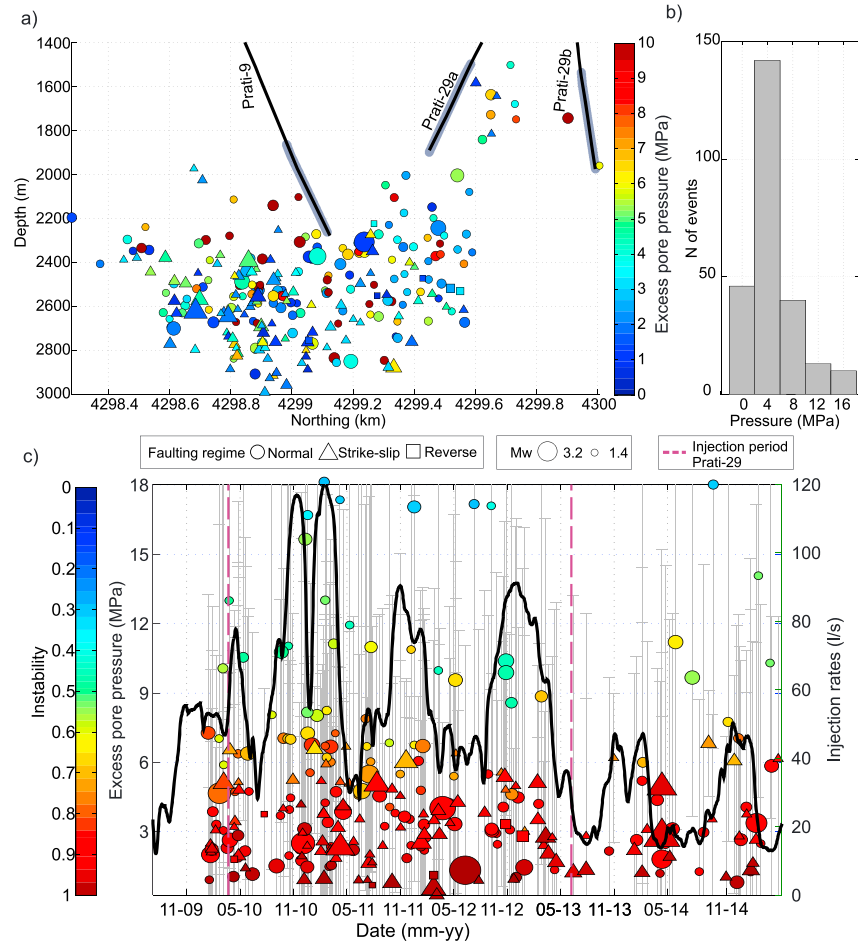
Figure 11. (a) Depth-northing distribution of the seismicity color encoded with their estimated excess pore pressure for reactivation. (b) Distributions of fluid pressures required for fault and fracture activation. (c) Temporal evolution of the estimated reactivation pressures (individual symbols corresponding to each event) and aggregated injection rates (black line) from both wells Prati-9 and Prati-29. Symbols are color encoded with the instability. Grey bars represent pore pressure uncertainty.

coefficient of $\mu = 0.5$ (optimum friction obtained from the instability analysis; see above) and the following expression:

$$\frac{S_1 - P^{hydros}}{S_3 - P^{hydros}} \leq \left(\sqrt{\mu^2 + 1} + \mu\right)^2 \tag{3}$$

In equation (3), we further assume hydrostatic pore pressure conditions prior to injection. The intermediate stress S_2 can be constrained from the stress ratio R (equation (1)). At reservoir depth (≈ 2.8 km) the absolute stress magnitudes S_1, S_2, and S_3 are estimated to be approximately 60, 54, and 40 MPa, respectively. We now calculate the corresponding shear and normal tractions acting on each fault plane, and subsequently, we estimate the change in pore pressure required to bring each fault to failure adopting a Mohr-Coulomb criterion:

$$\tau = C + \mu(\sigma_n - P) \tag{4}$$

where τ and σ_n represent the shear and normal tractions, respectively, μ is the coefficient of friction, and P is excess pore pressure. We assumed rock cohesion $C = 0$ MPa in agreement with the hypothesis that the microseismicity activated preexisting fractures and faults.

Our analysis indicates that for 91% of the fault planes failure would occur for a pore pressure increase <10 MPa (Figures 11a and 11b). These pressure changes are in good agreement with the estimates provided

by numerical thermohydromechanical modeling [*Rutqvist et al.*, 2013; *Jeanne et al.*, 2014a]. In addition, thermoelastic effects are expected to affect the local stresses near the injection wells allowing the reactivation of less favorable faults that would require larger excess pore pressures > 10 MPa. Most of these faults are located near or right below the open-hole section of both injection wells and in between the two wells, where the induced fluid pressures are expected to reach a maximum. However, the uncertainties of the excess pressure distribution derived from the uncertainties (see section 3.2) on the fault instability are very large, in many cases as large as the reported values. This is directly related to the large effect that the diversity of the acceptable focal mechanisms has for the fault instability.

The seismic events at low-instability faults are observed to occur mostly during periods of high injection rates especially when both wells are active thus increasing the pore fluid pressure in the reservoir (Figure 11c). The estimated pore pressure changes here are significantly smaller than those obtained at the Basel Deep Mining Project, which reached up to ≈ 30 MPa [*Terakawa et al.*, 2012; *Terakawa*, 2014]. However, those wellhead pressures were substantially larger than at The Geysers, where fluid flows into the reservoir by gravitational effects.

5.3. Other Potential Factors Enhancing Low-Instability Fault Reactivation

Throughout this study we have considered the possibility that the observed low-instability events could result from larger uncertainties in the inversion. However, most low-instability faults mainly display only slightly increased fault plane angular error. Other sources of error are possible. For example, assuming a homogeneous stress field will not capture local stress reorientation related to fault bends and step over regions. These local stress reorientations near some faults may result in normal faulting and reverse events at fault segments severely misoriented with regard to the far-field stress orientation. Another source of error may be the assumption of pure double-couple sources, which may not necessarily be appropriate for all the seismic events. Previous studies of The Geysers have found significant nondouble-couple component included in the $M \approx 3$ earthquakes [*Guilhem et al.*, 2014; *Boyd et al.*, 2015] or for the Enhanced Geothermal System in the northwestern part of the field [*Johnson*, 2014]. If low-instability events have significant non-double couple components, their fault plane orientations could be biased with respect to the now assumed pure double-couple solutions, resulting in slightly different instability values.

Finally, it is also possible that stress redistribution due to the occurrence of the larger earthquakes may have modified the stress conditions and/or frictional properties at these faults toward failure. While the role of stress transfer in fluid-induced seismicity was minor for Sôultz-sous-Fôrets [*Schoenball et al.*, 2012], it was found to agree with pore pressure triggering models at Basel [*Catalli et al.*, 2013].

6. Conclusions

We evaluated the orientation and geometry of reactivated faults and induced seismicity related to fluid injection activities at the northwestern part of The Geysers geothermal field using 304 high-quality focal mechanisms. We characterized fault geometry, instability coefficient *I*, and slip misfit angle β with respect to the local stress field. The focal mechanisms were derived from first-motion polarities using a refined hypocenter catalog and the HASH software. A statistical analysis allowed estimating most likely fault instabilities considering the uncertainties of both deviatoric stress tensor and focal mechanisms. The main findings of this study are as follows:

1. The fault plane orientations of the focal mechanisms show a large variability, and the majority of the events indicate oblique slip. Fault mechanisms include normal, strike-slip, and some reverse faulting in the selected seismicity cluster covering an area of about 1 km × 2 km and occurring at shallow depth ($<$3 km).
2. Fault instabilities of 72% of the fault planes are $I \geq 0.8$ indicating that they are favorably oriented for reactivation with respect to the stress field, but a number of seismic events with low instability are also observed. Many of the faults with high instability show large misfit angles between slip directions and shear traction vectors inferred from the stress inversion.
3. We found that the range of activated moment magnitudes is larger at higher fault instability and lower slip misfit angle. The largest events occur on optimally oriented faults displaying high instability and relatively small slip misfit angles. Favorably oriented faults also host larger earthquake activity, in good agreement with constant *b* value and larger *a* value.

4. For 91% of the analyzed data set, the pore pressure excess needed to reactivate these faults is $< 10\,$MPa, in agreement with previous estimates of combined thermal and pore pressure effects from fluid injection at The Geysers geothermal field. Events on more severely misoriented faults require larger pore pressures and occur around and below the open-hole sections of both wells and during periods of high injection rates.

References

Aagaard, B. T., J. L. Blair, J. Boatwright, S. H. Garcia, R. A. Harris, A. J. Michael, D. P. Schwartz, and J. S. DiLeo (2016), Earthquake outlook for the San Francisco Bay region 2014–2043 (ver. 1.1, August 2016), U.S. Geol. Surv. Fact Sheet 2016-3020, 6 p., doi:10.3133/fs20163020.

Aki, K., and P. G. Richards (2002), *Quantitative Seismology: Theory and Methods*, University Science Books, Herndon, Va.

Amitrano, D. (2003), Brittle-ductile transition and associated seismicity: Experimental and numerical studies and relationship with the *b* value, *J. Geophys. Res.*, *108*(B1), 2044, doi:10.1029/2001JB000680.

Bachmann, C. E., S. Wiemer, B. P. Goertz-Allmann, and J. Woessner (2012), Influence of pore-pressure on the event-size distribution of induced earthquakes, *Geophys. Res. Lett.*, *39*, L09302, doi:10.1029/2012GL051480.

Barbour, A. J. (2015), Pore pressure sensitivities to dynamic strains: Observations in active tectonic regions, *J. Geophys. Res. Solid Earth*, *120*, 5863–5883, doi:10.1002/2015JB012201.

Barton, C. A., M. D. Zoback, and D. Moos (1995), Fluid flow along potentially active faults in crystalline rock, *Geology*, *23*(8), 683–686, doi:10.1130/0091-7613(1995)023<0683:FFAPAF>2.3.CO;2.

Boyd, O. S., D. S. Dreger, V. H. Lai, and R. Gritto (2015), A systematic analysis of seismic moment tensor at The Geysers Geothermal Field, California, *Bull. Seismol. Soc. Am.*, doi:10.1785/0120140285.

Boyle, K., and M. Zoback (2011), Stress and fracture orientation in the NorthWest Geysers geothermal field, Proc. Thirty-Eight Workshop Geotherm. Reserv. Eng. Stanf. Univ. Stanf. Calif.

Boyle, K., and M. Zoback (2014), The stress state of the Northwest Geysers, California, geothermal field, and implications for fault-controlled fluid flow, *Bull. Seismol. Soc. Am.*, doi:10.1785/0120130284.

Catalli, F., M.-A. Meier, and S. Wiemer (2013), The role of Coulomb stress changes for injection-induced seismicity: The Basel enhanced geothermal system, *Geophys. Res. Lett.*, *40*, 72–77, doi:10.1029/2012GL054147.

Chen, X., and P. M. Shearer (2011), Comprehensive analysis of earthquake source spectra and swarms in the Salton Trough, California, *J. Geophys. Res.*, *116*, B09309, doi:10.1029/2011JB008263.

Cuenot, N., J. Charléty, L. Dorbath, and H. Haessler (2006), Faulting mechanisms and stress regime at the European HDR site of Soultz-sous-Forêts, France, *Geothermics*, *35*(5–6), 561–575, doi:10.1016/j.geothermics.2006.11.007.

Deichmann, N., and D. Giardini (2009), Earthquakes induced by the stimulation of an enhanced geothermal system below Basel (Switzerland), *Seismol. Res. Lett.*, *80*(5), 784–798, doi:10.1785/gssrl.80.5.784.

Eberhart-Phillips, D., and D. H. Oppenheimer (1984), Induced seismicity in The Geysers Geothermal Area, California, *J. Geophys. Res.*, *89*(B2), 1191–1207, doi:10.1029/JB089iB02p01191.

Ellsworth, W. L. (2013), Injection-induced earthquakes, *Science*, *341*(6142), 1225942, doi:10.1126/science.1225942.

Gephart, J. W., and D. W. Forsyth (1984), An improved method for determining the regional stress tensor using earthquake focal mechanism data: Application to the San Fernando Earthquake Sequence, *J. Geophys. Res. Solid Earth*, *89*(B11), 9305–9320, doi:10.1029/JB089iB11p09305.

Gischig, V. S. (2015), Rupture propagation behavior and the largest possible earthquake induced by fluid injection into deep reservoirs, *Geophys. Res. Lett.*, *42*, 7420–7428, doi:10.1002/2015GL065072.

Guilhem, A., L. Hutchings, D. S. Dreger, and L. R. Johnson (2014), Moment tensor inversions of *M* ~ 3 earthquakes in the Geysers geothermal fields, California, *J. Geophys. Res. Solid Earth*, *119*, 2121–2137, doi:10.1002/2013JB010271.

Hardebeck, J. L., and E. Hauksson (2001), Crustal stress field in southern California and its implications for fault mechanics, *J. Geophys. Res.*, *106*(B10), 21,859–21,882, doi:10.1029/2001JB000292.

Hardebeck, J. L., and A. J. Michael (2006), Damped regional-scale stress inversions: Methodology and examples for southern California and the Coalinga aftershock sequence, *J. Geophys. Res.*, *111*, B11310, doi:10.1029/2005JB004144.

Hardebeck, J. L., and P. M. Shearer (2002), A new method for determining first-motion focal mechanisms, *Bull. Seismol. Soc. Am.*, *92*(6), 2264–2276, doi:10.1785/0120010200.

Hickman, S., and M. Zoback (2004), Stress orientations and magnitudes in the SAFOD pilot hole, *Geophys. Res. Lett.*, *31*, L15S12, doi:10.1029/2004GL020043.

Ickrath, M., M. Bohnhoff, G. Dresen, P. Martínez-Garzón, F. Bulut, G. Kwiatek, and O. Germer (2015), Detailed analysis of spatiotemporal variations of the stress field orientation along the Izmit-Düzce rupture in NW Turkey from inversion of first-motion polarity data, *Geophys. J. Int.*, *202*(3), 2120–2132, doi:10.1093/gji/ggv273.

Jaeger, J., and N. G. Cook (1971), *Fundamentals of Rock Mechanics*, Springer, Malden, Mass.

Jeanne, P., J. Rutqvist, D. Vasco, J. Garcia, P. F. Dobson, M. Walters, C. Hartline, and A. Borgia (2014a), A 3D hydrogeological and geomechanical model of an enhanced geothermal system at The Geysers, California, *Geothermics*, *51*, 240–252, doi:10.1016/j.geothermics.2014.01.013.

Jeanne, P., J. Rutqvist, C. Hartline, J. Garcia, P. F. Dobson, and M. Walters (2014b), Reservoir structure and properties from geomechanical modeling and microseismicity analyses associated with an enhanced geothermal system at The Geysers, California, *Geothermics*, *51*, 460–469, doi:10.1016/j.geothermics.2014.02.003.

Johnson, L. R. (2014), Source mechanisms of induced earthquakes at The Geysers geothermal reservoir, *Pure Appl. Geophys.*, *171*(8), 1641–1668, doi:10.1007/s00024-014-0795-x.

Kwiatek, G., P. Martínez-Garzón, G. Dresen, M. Bohnhoff, H. Sone, and C. Hartline (2015), Effects of long-term fluid injection on induced seismicity parameters and maximum magnitude in northwestern part of The Geysers geothermal field, *J. Geophys. Res. Solid Earth*, doi:10.1002/2015JB012362.

Lund, B., and R. Slunga (1999), Stress tensor inversion using detailed microearthquake information and stability constraints: Application to Ölfus in southwest Iceland, *J. Geophys. Res.*, *104*(B7), 14,947–14,964, doi:10.1029/1999JB900111.

Majer, E. L., and J. E. Peterson (2007), The impact of injection on seismicity at The Geysers, California Geothermal Field, *Int. J. Rock Mech. Min. Sci.*, *44*(8), 1079–1090, doi:10.1016/j.ijrmms.2007.07.023.

Martínez-Garzón, P., M. Bohnhoff, G. Kwiatek, and G. Dresen (2013), Stress tensor changes related to fluid injection at The Geysers geothermal field, California, *Geophys. Res. Lett.*, *40*, 2596–2691, doi:10.1002/grl.50438.

Martínez-Garzón, P., G. Kwiatek, H. Sone, M. Bohnhoff, G. Dresen, and C. Hartline (2014), Spatiotemporal changes, faulting regimes, and source parameters of induced seismicity: A case study from The Geysers geothermal field, *J. Geophys. Res. Solid Earth*, *119*, 8378–8396, doi:10.1002/2014JB011385.

Martínez-Garzón, P., M. Bohnhoff, Y. Ben-Zion, and G. Dresen (2015), Scaling of maximum observed magnitudes with geometrical and stress properties of strike-slip faults, *Geophys. Res. Lett.*, *42*, 10,230–10,238, doi:10.1002/2015GL066478.

Martínez-Garzón, P., V. Vavryčuk, G. Kwiatek, and M. Bohnhoff (2016), Sensitivity of stress inversion of focal mechanisms to pore pressure changes, *Geophys. Res. Lett.*, *43*, 8441–8450, doi:10.1002/2016GL070145.

Martínez-Garzón, P., G. Kwiatek, M. Ickrath, and M. Bohnhoff (2014), MSATSI: A MATLAB package for stress inversion combining solid classic methodology, a new simplified user-handling, and a visualization tool, *Seismol. Res. Lett.*, *85*(4), 896–904, doi:10.1785/0220130189.

McGarr, A. (2014), Maximum magnitude earthquakes induced by fluid injection, *J. Geophys. Res. Solid Earth*, *119*, 1008–1019, doi:10.1002/2013JB010597.

Michael, A. J. (1984), Determination of stress from slip data: Faults and folds, *J. Geophys. Res.*, *89*(B13), 11,517–11,526, doi:10.1029/JB089iB13p11517.

Michael, A. J. (1987), Use of focal mechanisms to determine stress: A control study, *J. Geophys. Res.*, *92*(B1), 357–368, doi:10.1029/JB092iB01p00357.

Michael, A. J. (1991), Spatial variations in stress within the 1987 Whittier Narrows, California, aftershock sequence: New techniques and results, *J. Geophys. Res. Solid Earth*, *96*(B4), 6303–6319, doi:10.1029/91JB00195.

Moeck, I., G. Kwiatek, and G. Zimmermann (2009), Slip tendency analysis, fault reactivation potential and induced seismicity in a deep geothermal reservoir, *J. Struct. Geol.*, *31*(10), 1174–1182, doi:10.1016/j.jsg.2009.06.012.

Morris, A., D. A. Ferrill, and D. B. Henderson (1996), Slip-tendency analysis and fault reactivation, *Geology*, *24*(3), 275–278, doi:10.1130/0091-7613(1996)024<0275:STAAFR>2.3.CO;2.

Murray, J. R., S. E. Minson, and J. L. Svarc (2014), Slip rates and spatially variable creep on faults of the northern San Andreas system inferred through bayesian inversion of global positioning system data, *J. Geophys. Res. Solid Earth*, *119*, 6023–6047, doi:10.1002/2014JB010966.

Örgülü, G. (2011), Seismicity and source parameters for small-scale earthquakes along the splays of the North Anatolian Fault (NAF) in the Marmara Sea, *Geophys. J. Int.*, *184*(1), 385–404, doi:10.1111/j.1365-246X.2010.04844.x.

Rutqvist, J., P. F. Dobson, J. Garcia, C. Hartline, P. Jeanne, C. M. Oldenburg, D. W. Vasco, and M. Walters (2013), The Northwest Geysers EGS demonstration project, California: Pre-stimulation modeling and interpretation of the stimulation, *Math. Geosci.*, *47*(1), 3–29, doi:10.1007/s11004-013-9493-y.

Schoenball, M., C. Baujard, T. Kohl, and L. Dorbath (2012), The role of triggering by static stress transfer during geothermal reservoir stimulation, *J. Geophys. Res.*, *117*, B09307, doi:10.1029/2012JB009304.

Scholz, C. H. (2002), *The Mechanics of Earthquakes and Faulting*, 2nd ed., Cambridge Univ. Press.

Shapiro, S. A., R. Patzig, E. Rothert, and J. Rindschwentner (2003), Triggering of seismicity by pore-pressure perturbations: Permeability-related signatures of the phenomenon, *Pure Appl. Geophys.*, *160*(5–6), 1051–1066, doi:10.1007/PL00012560.

Sibson, R. H. (1985), A note on fault reactivation, *J. Struct. Geol.*, *7*(6), 751–754, doi:10.1016/0191-8141(85)90150-6.

Sibson, R. H. (1990), Rupture nucleation on unfavorably oriented faults, *Bull. Seismol. Soc. Am.*, *80*(6A), 1580–1604.

Sibson, R. H. (2014), Earthquake rupturing in fluid-overpressured crust: How common?, *Pure Appl. Geophys.*, *171*(11), 2867–2885, doi:10.1007/s00024-014-0838-3.

Terakawa, T. (2014), Evolution of pore fluid pressures in a stimulated geothermal reservoir inferred from earthquake focal mechanisms, *Geophys. Res. Lett.*, *41*, 7468–7476, doi:10.1002/2014GL061908.

Terakawa, T., S. A. Miller, and N. Deichmann (2012), High fluid pressure and triggered earthquakes in the enhanced geothermal system in Basel, Switzerland, *J. Geophys. Res.*, *117*, B07305, doi:10.1029/2011JB008980.

Terakawa, T., Y. Yamanaka, H. Nakamichi, T. Watanabe, F. Yamazaki, S. Horikawa, and T. Okuda (2013), Effects of pore fluid pressure and tectonic stress on diverse seismic activities around the Mt. Ontake volcano, central Japan, *Tectonophysics*, *608*, 138–148, doi:10.1016/j.tecto.2013.10.005.

Townend, J., S. Sherburn, R. Arnold, C. Boese, and L. Woods (2012), Three-dimensional variations in present-day tectonic stress along the Australia–Pacific plate boundary in New Zealand, *Earth Planet. Sci. Lett.*, *353–354*, 47–59, doi:10.1016/j.epsl.2012.08.003.

Vavryčuk, V. (2011), Principal earthquakes: Theory and observations for the 2008 West Bohemia swarm, *Earth Planet. Sci. Lett.*, *305*(3–4), 290–296, doi:10.1016/j.epsl.2011.03.002.

Vavryčuk, V. (2014), Iterative joint inversion for stress and fault orientations from focal mechanisms, *Geophys. J. Int.*, *199*(1), 69–77, doi:10.1093/gji/ggu224.

Vavryčuk, V. (2015), Earthquake mechanisms and stress field, in *Encyclopedia of Earthquake Engineering*, edited by M. Beer et al., pp. 728–746, Springer, Berlin.

Vavryčuk, V., F. Bouchaala, and T. Fischer (2013), High-resolution fault image from accurate locations and focal mechanisms of the 2008 swarm earthquakes in West Bohemia, Czech Republic, *Tectonophysics*, *590*, 189–195, doi:10.1016/j.tecto.2013.01.025.

Waldhauser, F., and W. L. Ellsworth (2000), A double-difference earthquake location algorithm: Method and application to the Northern Hayward Fault, California, *Bull. Seismol. Soc. Am.*, *90*(6), 1353–1368, doi:10.1785/0120000006.

Waldhauser, F., and D. P. Schaff (2008), Large-scale relocation of two decades of Northern California seismicity using cross-correlation and double-difference methods, *J. Geophys. Res.*, *113*, B08311, doi:10.1029/2007JB005479.

Weingarten, M., S. Ge, J. W. Godt, B. A. Bekins, and J. L. Rubinstein (2015), High-rate injection is associated with the increase in U.S. mid-continent seismicity, *Science*, *348*(6241), 1336–1340, doi:10.1126/science.aab1345.

Woessner, J., and S. Wiemer (2005), Assessing the quality of earthquake catalogues: Estimating the magnitude of completeness and its uncertainty, *Bull. Seismol. Soc. Am.*, *95*(2), 684–698, doi:10.1785/0120040007.

Xu, S.-S., A. F. Nieto-Samaniego, and S. A. Alaniz-Álvarez (2010), 3D Mohr diagram to explain reactivation of pre-existing planes due to changes in applied stresses, International Society for Rock Mechanics.

Yang, W., E. Hauksson, and P. M. Shearer (2012), Computing a large refined catalog of focal mechanisms for Southern California (1981–2010): Temporal stability of the style of faulting, *Bull. Seismol. Soc. Am.*, *102*(3), 1179–1194, doi:10.1785/0120110311.

Zoback, M. D. (2007), *Reservoir Geomechanics*, Cambridge Univ. Press, Cambridge.

Zoback, M. D., S. Hickman, W. Ellsworth, and the SAFOD Science Team (2011), Scientific drilling into the San Andreas fault zone—An overview of SAFOD's first five years, *Sci. Drill.*, doi:10.2204/iodp.sd.11.02.2011.